

# Deep level defect spectroscopies of complex oxide surfaces and interfaces <sup>EP</sup>

Cite as: J. Vac. Sci. Technol. A **39**, 063215 (2021); <https://doi.org/10.1116/6.0001339>

Submitted: 06 August 2021 • Accepted: 30 September 2021 • Published Online: 20 October 2021

Jun Zhang, Kyle McNicholas, Snjezana Balaz, et al.

## COLLECTIONS

Paper published as part of the special topic on [Honoring Dr. Scott Chambers' 70th Birthday and His Leadership in the Science and Technology of Oxide Thin Films](#)

<sup>EP</sup> This paper was selected as an Editor's Pick



View Online



Export Citation



CrossMark

## ARTICLES YOU MAY BE INTERESTED IN

### Diffusion of dopants and impurities in $\beta$ -Ga<sub>2</sub>O<sub>3</sub>

Journal of Vacuum Science & Technology A **39**, 060801 (2021); <https://doi.org/10.1116/6.0001307>

### Practical guide for curve fitting in x-ray photoelectron spectroscopy

Journal of Vacuum Science & Technology A **38**, 061203 (2020); <https://doi.org/10.1116/6.0000377>

### Review Article: Stress in thin films and coatings: Current status, challenges, and prospects

Journal of Vacuum Science & Technology A **36**, 020801 (2018); <https://doi.org/10.1116/1.5011790>



Instruments for **Advanced Science**

- Knowledge,
- Experience,
- Expertise

Click to view our product catalogue

Contact Hiden Analytical for further details:  
[www.HidenAnalytical.com](http://www.HidenAnalytical.com)  
[info@hideninc.com](mailto:info@hideninc.com)

Gas Analysis

- ▶ dynamic measurement of reaction gas streams
- ▶ catalysis and thermal analysis
- ▶ molecular beam studies
- ▶ dissolved species probes
- ▶ fermentation, environmental and ecological studies

Surface Science

- ▶ UHVTPD
- ▶ SIMS
- ▶ end point detection in ion beam etch
- ▶ elemental imaging - surface mapping

Plasma Diagnostics

- ▶ plasma source characterization
- ▶ etch and deposition process reaction kinetic studies
- ▶ analysis of neutral and radical species

Vacuum Analysis

- ▶ partial pressure measurement and control of process gases
- ▶ reactive sputter process control
- ▶ vacuum diagnostics
- ▶ vacuum coating process monitoring

# Deep level defect spectroscopies of complex oxide surfaces and interfaces

Cite as: J. Vac. Sci. Technol. A 39, 063215 (2021); doi: 10.1116/6.0001339

Submitted: 6 August 2021 · Accepted: 30 September 2021 ·

Published Online: 20 October 2021



Jun Zhang,<sup>1</sup> Kyle McNicholas,<sup>2</sup> Snjezana Balaz,<sup>3</sup> Zhao Quan Zeng,<sup>4</sup> Darrell Schlom,<sup>5,6</sup> and Leonard J. Brillson<sup>7,8,a)</sup> 

## AFFILIATIONS

<sup>1</sup>Spears School of Business, Oklahoma State University, Stillwater, Oklahoma 74078

<sup>2</sup>MIT Lincoln Laboratories, Lexington, Massachusetts 02421

<sup>3</sup>Department of Physics, Astronomy, Geology, and Environmental Science, Youngstown State University, Youngstown, Ohio 44555

<sup>4</sup>II-VI Incorporated, Warren, Pennsylvania 07059

<sup>5</sup>Department of Materials Science and Engineering, Cornell University, Ithaca, New York 14853

<sup>6</sup>Kavli Institute at Cornell for Nanoscale Science, Ithaca, New York 14853

<sup>7</sup>Department of Electrical and Computer Engineering, The Ohio State University, Columbus, Ohio 43210

<sup>8</sup>Department of Physics, The Ohio State University, Columbus, Ohio 43210

**Note:** This paper is a part of the Special Collection Honoring Dr. Scott Chambers' 70th Birthday and His Leadership in the Science and Technology of Oxide Thin Films.

**a)** Author to whom correspondence should be addressed: [brillson.1@osu.edu](mailto:brillson.1@osu.edu)

## ABSTRACT

Intrinsic point defects are commonly present in and can strongly affect the electronic properties of complex oxides and their interfaces. The near- and subsurface characterization techniques, depth-resolved cathodoluminescence spectroscopy and surface photovoltage spectroscopy, can measure the density distributions, energy levels, and optical transitions of intrinsic point defects in complex oxides on a near-nanometer scale. These measurements on SrTiO<sub>3</sub>, BaTiO<sub>3</sub>, and related materials reveal the sensitivity of intrinsic point defects to growth temperature, mechanical strain, crystal orientation, and chemical interactions. Spatial redistribution of these defects can vary significantly near surfaces and interfaces and can have strong electronic effects. The combination of these deep level spectroscopies along with other advanced characterization techniques provides an avenue to further expand the understanding and control of complex oxide defects in general.

Published under an exclusive license by the AVS. <https://doi.org/10.1116/6.0001339>

## I. INTRODUCTION

Complex oxides have emerged as exciting electronic materials over the past two decades due to their wide array of electromagnetic properties, particularly in ultrathin films and at their interfaces. The discovery of high conductivity at otherwise insulating complex oxide interfaces has attracted considerable interest in understanding their intrinsic physics and materials science.<sup>1–6</sup> Extensive studies of complex oxides over the past decade have shown how sensitive their electronic properties are to specific epitaxial growth conditions, particularly at atomic-scale interfaces between epitaxially grown oxides. Thus, Chambers *et al.* showed that complex oxide interfaces can exhibit chemical interactions,<sup>7–10</sup>

just as Brillson *et al.* showed that such interface chemical reactions are common and systematic at metal-compound semiconductor interfaces.<sup>11,12</sup> As expressed in Chambers's Advanced Materials review, "Future scientific growth in this field depends critically on our ability to monitor and control both oxide epitaxial film growth processes and the film and interface structure and composition."<sup>13</sup>

Due to their electrical activity, intrinsic point defects can strongly affect the electronic properties of complex oxide thin films and their interfaces. Extensive growth and transport studies have revealed the high sensitivity of such defects to epitaxial growth processes and chemical interactions on the atomic scale. We now know that intrinsic point defects are present in high densities

within complex oxide semiconductors and insulators. These densities can be large enough to dominate free carrier densities, form significant dipoles at interfaces, and introduce conductive channels both at interfaces and across bulk films. In this article, we show how depth-resolved cathodoluminescence spectroscopy (DRCLS)<sup>14–16</sup> and surface photovoltage spectroscopy (SPS),<sup>17–19</sup> both near-surface and subsurface characterization techniques, can measure the density distributions, energy levels, and optical transitions of such defects on a near-nanometer scale. These measurements reveal the sensitivity of intrinsic point defects to growth temperature, mechanical strain, crystal orientation, and chemical interactions.

Measuring the physical nature, densities, and spatial distribution of these defects is challenging for most characterization methods due to the ultrathin dimensions of complex oxide films grown epitaxially on lattice-matched substrates. Thus, otherwise widely used capacitance techniques such as deep level transient spectroscopy and its variants are limited by the depletion regions involved, which can easily exceed film thicknesses. Spin-sensitive magnetic techniques such as electron paramagnetic resonance (EPR) and optically detected magnetic resonance are limited by the minimum number of spins required for detection, typically  $>10^{11}$ , and the absence of depth resolution. Optical spectroscopies are limited by 100 nm scale and poorer depth resolution, electrical spectroscopies by both poor depth resolution and the insulating nature of undoped complex oxides, and magnetic spectroscopies by the minimum material volumes at given spin densities required for detection. Cathodoluminescence spectroscopy (CLS)<sup>20</sup> and DRCLS achieve both state-of-the-art sensitivity to defect densities, e.g.,  $<10^{15} \text{ cm}^{-3}$ , as well as near-nanometer depth and lateral resolution. Furthermore, the incident electron beam enables excitation of optical emission with above bandgap energies exceeding those of lasers and other optical sources. This combination of sensitivity, nanometer-scale spatial resolution in three dimensions, and above bandgap excitation is very well suited to explore intrinsic point defects in complex oxides, where the presence and spatial distribution of charged imperfections and impurities at the nanoscale can determine the macroscopic electronic and magnetic properties of these materials.

After cathodoluminescence spectroscopy studies first made use of depth-resolved measurements in semiconductors,<sup>21</sup> Brillson *et al.* applied DRCLS to study defects at ultrahigh vacuum (UHV)-cleaved surfaces of conventional semiconducting materials to examine their role in Schottky barrier formation.<sup>22–24</sup> The extension of DRCLS to wide bandgap semiconductors demonstrated the role of interface-specific defects and chemical interactions in controlling Schottky barrier formation.<sup>25,26</sup> The discovery of conducting interfaces between otherwise insulating electronic materials motivated the extension of DRCLS interface studies to a wide range of complex oxides.<sup>27–32</sup>

DRCLS together with SPS provide the ability to measure optical transitions associated with deep level defects but also to determine the energies of these deep levels with respect to the semiconductor's valence and conduction bands. Together with theoretical predictions of energy levels for specific defects, this information can help identify the physical nature of these defects. The intensity and physical redistribution behavior of these defects with thermal and chemical processing can provide further evidence to

support such defect identification. And the measurement of these defects inside actual devices, even during operation, can help us understand electronic behavior at the nanoscale.<sup>33</sup>

This article is structured as follows: Section II provides brief descriptions of the DRCLS and SPS techniques. Section III describes the application of these techniques to measure and identify deep level defects in SrTiO<sub>3</sub>, BaTiO<sub>3</sub>, and related materials. These results also show how specific defect densities and spatial distributions depend on chemical processing, growth stoichiometry, and epitaxial strain. Section IV discusses how these defects spatially redistribute due to orientation-dependent intrinsic electric fields and externally applied bias. Section V discusses the impact of specific defects in complex oxide electronic structures. Section VI discusses new directions for studies of intrinsic point defects in complex oxides.

## II. EXPERIMENTAL TECHNIQUES

The DRCLS technique involves an incident electron beam that generates a cascade of secondary electrons by scattering with the semiconductor or the insulator lattice. Depending on the incident beam energy, these electrons lose energy sequentially to x rays, plasmons, and finally, electron-hole (e-h) pairs.<sup>34</sup> Monte Carlo simulations including backscattering can provide depth distributions of the final positions of these electrons,<sup>35,36</sup> which correspond to the energies of e-h excitation,<sup>37</sup> recombination, and light emission to within the few Å scattering length of these final, low-energy electrons.<sup>38</sup> For incident beam energies ranging from 0.1 to 5 keV, excitation depths range from the sub-10 nm to the several 100-nm scale, depending on the density, atomic weight, and atomic number of the target lattice.<sup>39,40</sup> The excited electrons and holes can recombine *via* band-to-band, band-to-defect, and defect-to-band transitions with a range of momenta. DRCLS can also detect higher lying conduction band transitions to the valence band maximum, given the relatively high incident beam energy.

SPS involves a vibrating Kelvin probe whose high impedance feedback circuit continuously monitors the electric potential difference between the probe and the sample surface as a function of increasing incident photon beam energy. The onset of photo-stimulated population of electrons from the valence band into states within a semiconductor or an insulator bandgap changes the initial surface band bending, the surface electric potential, and the contact potential difference (cpd) measured by the Kelvin probe circuit. Likewise, the onset of photo-stimulated depopulation from a state within the bandgap to the conduction band results in an opposite sign of band bending change, surface potential, and measured cpd. The onset of these transitions produces a slope change in cpd versus photon energy  $h\nu$  at energies that correspond to the transition energy involved. Furthermore, the sign of slope change indicates the photopopulation or depopulation nature of the transition. The energy and sign of cpd slope change provide the position of a given defect level within the bandgap. Then by combining SPS with DRCLS intensity versus depth profiles of the same optical transition, one can determine both a specific defect's energy level within the band and the depth distribution of that defect.

For DRCLS studies, we used an ultrahigh vacuum (UHV) chamber with a glancing incidence electron gun with constant

beam current of 2 mA and incident beam voltages  $E_B = 0.1\text{--}5$  keV. The optical detection system consisted of a  $\text{CaF}_2$  focusing lens inside the UHV chamber, a sapphire viewport, an  $f$ -number matcher, a grating monochromator, and a charge couple detector (CCD). For SPS, we used a Park Systems XE-70 High Accuracy Small Sample probe microscope SPM in noncontact mode with conductive Cr-Au cantilever tips to perform electrostatic force microscopy, i.e., Kelvin probe force microscopy (KPFM). We used a Stanford Research Systems SR830 lock-in amplifier to apply an additional 17–18 kHz AC voltage to isolate the electrostatic signal. For KPFM, a variable DC tip bias is controlled with a lock-in amplifier feedback to null out the potential difference between the tip and the surface.

The  $\text{SrTiO}_3$  samples that we studied were both commercially available single crystals and thin films grown by molecular beam epitaxy (MBE). The MBE samples were grown under a variety of controlled temperature, plasma-assisted oxygen, stoichiometry, and substrate conditions. Unless otherwise noted,  $\text{SrTiO}_3$  films were epitaxially grown on  $\text{SrTiO}_3$  substrates under  $5 \times 10^{-7}$  Torr  $\text{O}_2$  with 10%  $\text{O}_3$  at a substrate temperature of 650 °C. The  $\text{SrTiO}_3$  single crystal substrates were chemically cleaned using a standard substrate pretreatment method. No further processing was made for the unprocessed substrates, and the processed substrates were further annealed at the thin film growth condition for 100 min.  $(\text{Ba,Sr})\text{TiO}_3$  samples were grown by either MBE or pulsed laser deposition (PLD). For MBE growth, we grew 100 nm  $(\text{Ba,Sr})\text{TiO}_3$  epilayers on  $\text{SrTiO}_3$  substrates by alternate deposition of Sr, Ba, and Ti layers. The  $\text{TiO}_2$ -terminated  $\text{SrTiO}_3$  (100) substrates were treated with an aqua regia etch prior to  $(\text{Ba,Sr})\text{TiO}_3$  deposition.<sup>41</sup> Source flux was calibrated by a quartz crystal microbalance and then by measuring *in situ* reflection high energy electron diffraction oscillations from a calibration sample grown in a 200 W,  $5 \times 10^{-7}$  Torr oxygen plasma

pressure ( $\text{PO}_2$ ) at  $T_G = 800$  °C. Films were grown with multiple, specific  $\text{PO}_2$  and substrate temperatures as indicated below.<sup>42</sup>  $\text{SrTiO}_3$  DRCLS was performed with samples cooled with a helium cryotip to  $\sim 43$  K. For PLD growth, we grew  $\text{Ba}_{0.5}\text{Sr}_{0.5}\text{TiO}_3$  with either 1  $\mu\text{m}$  thickness on MgO substrates with high (100) orientation, which exhibited high dielectric loss, or on randomly oriented  $\text{Ba}_{0.5}\text{Sr}_{0.5}\text{TiO}_3$  on Mg substrates with 1% W, which exhibited lower dielectric loss.<sup>43–45</sup>

### III. DEFECT MEASUREMENT AND IDENTIFICATION

Defects in complex oxides such as  $\text{SrTiO}_3$ ,  $\text{BaTiO}_3$ , and related materials exhibit strong variations in DRCLS intensity and spatial distribution with growth conditions and subsequent processing. These systematic variations can help identify the physical nature of specific defects. Figure 1 illustrates DRCL spectra with representative  $\text{SrTiO}_3$  bulk features. Figure 1(a) illustrates spectra from a commercially available  $\text{SrTiO}_3$  bulk crystal with  $E_B = 1\text{--}5$  kV. Monte Carlo simulations yield maximum excitation depths, i.e., Bohr-Bethe ranges  $R_B$ , based on the kinetic energy decrease of an energetic incident electron along its path length after multiple scattering events and the electron's final position in depth.<sup>46</sup> This final depth increases from 20 to 210 nm with increasing  $E_B$  as indicated. In Fig. 1(a), these spectra appear relatively unchanged with increasing excitation depth, consistent with bulk crystal uniformity. Optical emissions ranging from  $\sim 3.2$  eV bandgap down to  $\sim 1.4$  eV CCD cutoff show evidence of defect emissions at  $\sim 1.6$ , 2.1, and 2.6 eV. Defect emissions at 2.1 and 2.6 eV have intensities in excess of bandgap emission intensity, indicating relative high defect densities.

Spectral features above  $\sim 3.2$  eV bandgap correspond to optical transitions from higher lying conduction bands to the valence band edge. The broadness of defect emissions is attributed to multiple

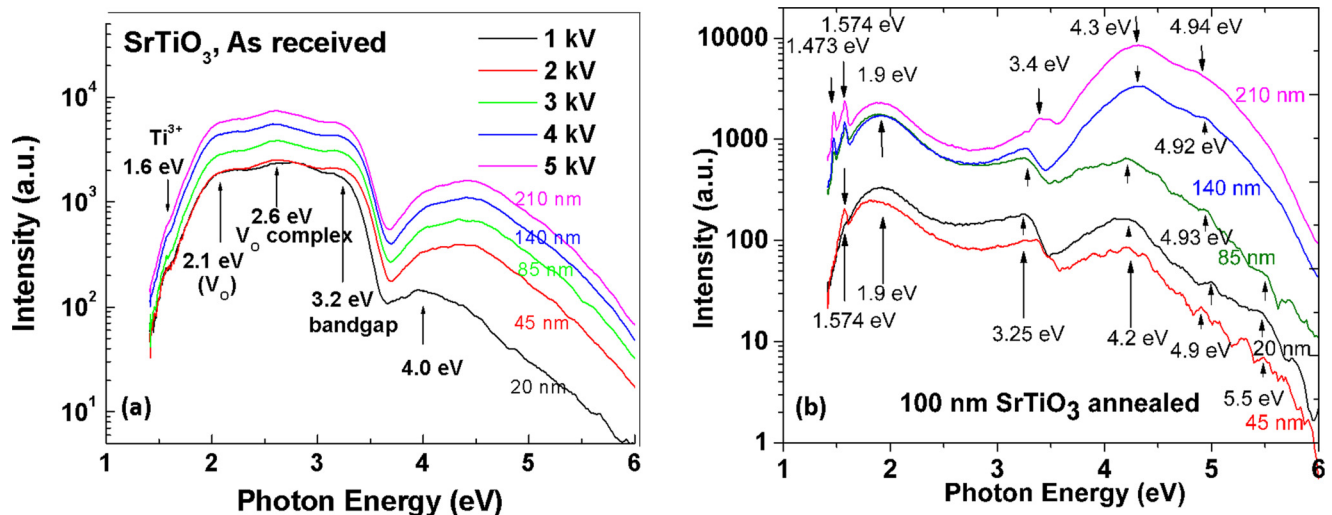


FIG. 1. DRCL spectra of (a) bulk, single-crystal  $\text{SrTiO}_3$  and (b) a 100 nm  $\text{SrTiO}_3$  epilayer on bulk  $\text{SrTiO}_3$ . Each colored spectrum corresponds to an incident electron beam energy  $E_B$  in kV and its corresponding maximum excitation depth  $R_B$  in nm as indicated. The depth dependence in (b) shows the spectral transition from an epilayer to the substrate.

defect sites within the SrTiO<sub>3</sub> lattice and possible defect clustering. Broadness of higher energy features is attributed to integration of above bandgap bands with momenta across the Brillouin zone, weighted by their densities of states.

Figure 1(b) illustrates DRCL spectra with representative SrTiO<sub>3</sub> MBE-grown epilayer features after 650 °C growth at  $5 \times 10^{-7}$  Torr O<sub>2</sub> (10% O<sub>3</sub>) followed by a 1 h, 700 °C O<sub>2</sub> anneal. The higher quality MBE-grown SrTiO<sub>3</sub> is evident from the lower deep level emissions compared to ~3.25 eV bandgap, particularly the decreased defect emission in the  $h\nu = 2\text{--}3$  eV region and the clearly defined emissions between 1.4 and 1.6 eV. Above bandgap features extending to the 6 eV CCD cutoff correspond to specific electronic transitions between three of four crystal field-split Ti 3d t<sub>2g</sub> orbital bands and the O 2p-derived valence band maximum. Table I provides a comparison of Fig. 1(b) features with interband transition energies measured by vacuum ultraviolet (VUV) spectroscopy and spectroscopic ellipsometry (SE) and predicted theoretically.<sup>47</sup> For each transition, VUV, SE, and DRCLS energies agree to within less than the spectroscopic uncertainties of <0.1 eV, supporting the precision of DRCLS energies across the full spectral range. DRCL spectra obtain similar agreement with theoretical band structure transition energies in, e.g., V<sub>2</sub>O<sub>5</sub><sup>48</sup> and ScN.<sup>49</sup>

Figure 1(b) also shows qualitative changes in subbandgap versus above-bandgap intensities with increasing depth, starting at 85 nm, consistent with the 100 nm depth of the epilayer-substrate interface versus the calculated Monte Carlo penetration depth and the higher substrate defect intensities versus the above bandgap bulk conduction band features.

The identification of specific defects with the spectral energies shown in Figs. 1(a) and 1(b) is based on earlier studies of defects in TiO<sub>2</sub>. The correspondence between defect features in SrTiO<sub>3</sub> and TiO<sub>2</sub> is possible because the valence bands of both SrTiO<sub>3</sub> and TiO<sub>2</sub> are derived entirely from O<sup>2-</sup> 2p states while the lowest unoccupied conduction bands of each are derived from Ti<sup>3+</sup> t<sub>2g</sub> states.<sup>50</sup> Early photo- and cathodoluminescence spectroscopies of sintered TiO<sub>2</sub> identified emissions at 0.85 μm (1.46 eV) and 0.82 μm (1.51 eV) with Ti<sup>3+</sup> interstitials in TiO<sub>2</sub> based the correlation of photoconductivity, photoluminescence, thermoluminescence, and thermally stimulated current ionization energies with the optical transition energies expected within the Ti<sup>3+</sup> ion in interstitial sites having nearly octahedral coordination.<sup>51</sup> A similar interpretation was given for both high temperature annealed rutile and anatase TiO<sub>2</sub>.<sup>52</sup> However, photoinduced EPR identified titanium-associated electron traps in TiO<sub>2</sub> crystals (rutile) with singly ionized and neutral oxygen vacancies whose unpaired spins are localized on two neighboring titanium

ions.<sup>53</sup> The TiO<sub>6</sub> octahedra common to both TiO<sub>2</sub> and SrTiO<sub>3</sub> led to identifying similar emissions in SrTiO<sub>3</sub> with Ti<sup>3+</sup> sites as well.<sup>52,54,55</sup> Hence, these emissions in SrTiO<sub>3</sub> are properly termed Ti<sup>3+</sup> ions on TiO<sub>6</sub> octahedral lattice sites. Likewise, sintering and photoemission studies suggested that losing oxygen atoms from the TiO<sub>6</sub> octahedra introduced states at 2.19 and 2.6 eV that were attributed to oxygen vacancies V<sub>O</sub> and V<sub>O</sub> complexes, respectively,<sup>55,56</sup> while ~2.9 eV emission has been attributed to self-trapped excitons<sup>56</sup> or V<sub>O</sub> complexes as well. Indeed, photoinduced EPR studies demonstrate V<sub>O</sub> with unpaired spins localized on two neighboring titanium Ti<sup>3+</sup> and a Ti<sup>3+</sup> self-trapped electron, and a self-trapped hole shared by two adjacent oxygen ions.<sup>53</sup> Isolated substitutional Fe<sup>3+</sup>, Al<sup>3+</sup>, and Cr<sup>3+</sup> ion impurities<sup>57,58</sup> are common in bulk SrTiO<sub>3</sub> and can form multiple deep levels with different charge states. For Fe, several of these charge states include Fe<sup>4+/5+</sup>V<sub>O</sub>, Fe<sup>3+/4+</sup>, and Fe<sup>2+/3+</sup>V<sub>O</sub> located 0.75, 1.06, and 1.35 eV above E<sub>v</sub>, respectively.<sup>58</sup> Their CL emissions exhibit narrow linewidths in contrast to the broader linewidths of intrinsic defect and band-to-band transitions presented in this study. For Fe impurities in SrTiO<sub>3</sub>, their energies differ significantly from those of the intrinsic defects reported here as does their appearance as a multiple charge state group. See also supplemental information.<sup>82</sup>

Thermal annealing MBE-grown SrTiO<sub>3</sub> produces DRCL spectral changes that support their identification with oxygen vacancies. Figure 2 shows spectra for 100 nm Sr<sub>1.2</sub>TiO<sub>3</sub> before and after a 700 °C, 1 h O<sub>2</sub> anneal. Previous DRCLS studies showed that Sr-rich growth increased defect emissions attributed to oxygen vacancies. Figure 2(a) shows that these Sr<sub>1.2</sub>TiO<sub>3</sub> emission intensities normalized to the 3.27 eV near band edge (NBE) increased by nearly an order of magnitude over those for SrTiO<sub>3</sub> in Fig. 1(b). Figure 2(b) shows how the O<sub>2</sub> anneal decreased defect emissions in the 2–3.3 eV range back to the range of SrTiO<sub>3</sub> normalized values, confirming the correlation with V<sub>O</sub>-related defects.

Based on Fig. 2, Table II shows that the dominant 2.0 eV emission decreased by 5.3× within the outer 20 nm, by 4.0× within the outer 45 nm, and by 2.1× within the outer 85 nm of the 100 nm epilayer. Likewise, the 2.6 eV emission strength decreased by 3.5× within the outer 20 nm, 3.8× within the outer 45 nm, and by 2.3× within the outer 85 nm. Table II indicates that these emissions all involve oxygen vacancy-related defects. Furthermore, the progression of highest to lowest defect reduction with increasing depth indicates that the removal of V<sub>O</sub> defect emissions occurs by diffusion of oxygen from the free surface into the bulk. In addition, the more pronounced reduction of 2.0 eV defect emission within the outer 20 nm suggests that it relates to a different V<sub>O</sub>-related defect, possibly isolated V<sub>O</sub> rather than a V<sub>O</sub>-related complex. Similar analysis of stoichiometric SrTiO<sub>3</sub> subbandgap defect emissions by the same high temperature oxygen anneal also shows reduction of both 2.0 and 2.6 eV defect emissions at 45 and 85 nm depths.

Mechanical strain introduced during epitaxial growth can strongly affect defects in complex oxides. Figure 3 shows deep level defect spectra for epilayer SrTiO<sub>3</sub> grown at different temperatures on substrates with varying lattice matches and strains. With higher growth temperature, more V<sub>O</sub>-related defects are expected as O incorporation in the epilayers during growth decreases. The orders-of-magnitude increase in defect emissions with increasing temperature supports this expectation.

**TABLE I.** Comparison of interband transition energies measured by VUV, SE, and CLS techniques.

Transition assignment	Technique <sup>46</sup>	Energy (eV)	DRCLS (eV)
Bandgap (indirect)	SE	3.25	3.25–3.27
O2p → Ti 3d t <sub>2g</sub>	SE/VUV	4.2/4.2	4.2–4.3
O2p → Ti 3d t <sub>2g</sub>	SE/VUV	4.9/4.8	4.9–4.94
O2p → Ti 3d t <sub>2g</sub>	SE/VUV	5.4/5.3	5.5
O2p → Ti 3d t <sub>2g</sub>	SE/VUV	6.3/6.3	Out of range

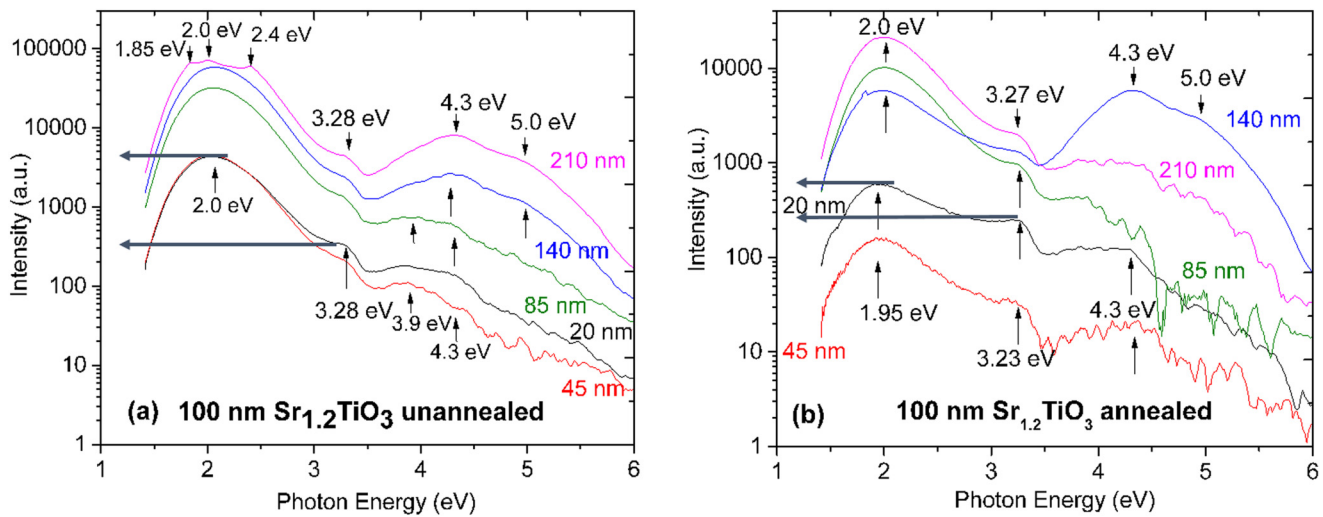


**FIG. 2.** DRCL spectra of 100 nm  $\text{Sr}_{1.2}\text{TiO}_3$  (a) before vs (b) after a 700 °C, 1 h  $\text{O}_2$  anneal. Annealing reduces subbandgap defect emissions in the  $h\nu = 2\text{--}3.27$  eV energy range, indicating oxygen vacancy-related defects. Each colored spectrum corresponds to a maximum excitation depth  $R_B$  in nm as indicated.

The substrate dependence of these spectra also highlights a strong dependence of defect densities on epitaxial strain.  $(\text{LaAlO}_3)_{0.3}(\text{Sr}_2\text{TaAlO}_6)_{0.7}$  (LSAT),  $\text{SrTiO}_3$  (STO) and  $\text{DyScO}_3$  (DSO) all have the perovskite crystal structure and are commonly used as single crystal substrates for the growth of epitaxial complex oxide films. Substrate lattice spacings  $a_o$  for (LSAT), (STO), and (DSO) are 3.868, 3.905, and 3.952 Å, respectively. Epitaxial lattice match to these substrates with increasing lattice spacing introduces increasing tensile strain in the 100 nm overlayers. Lattice atom spacing can increase or decrease  $\text{Ti}^{3+}$  repulsion, making  $\text{V}_\text{O}$  formation more or less likely. Missing O atoms between Ti atoms introduces more  $\text{Ti}^{3+}\text{--Ti}^{3+}$  repulsion, increasing their separation and expanding the lattice.

Conversely, increased lattice spacing renders  $\text{V}_\text{O}$  formation more energetically favorable. The apparent  $\text{Ti}^{3+}$ -related defect increase in Fig. 3(c) is consistent with such increased  $\text{V}_\text{O}$  formation and the correlation of  $\text{V}_\text{O}$  with neighboring  $\text{Ti}^{3+}$  atoms.<sup>57</sup> Previously, studies of  $\text{SrTiO}_3$  sintering established an increase in oxygen vacancies and increased lattice parameters with decreasing oxygen partial pressure.<sup>59</sup> For  $\text{SrTiO}_3$  grown at 650 °C, Fig. 3(c) also shows that  $\text{Ti}^{3+}$ -related normalized emission intensities increase with increasing tensile strain, consistent with increased  $\text{V}_\text{O}$  density, even for this lowest growth temperature. For the 1000 °C

$\text{V}_\text{O}$ -rich growth, the compressive strain introduced by the LSAT substrate depresses both  $\text{Ti}^{3+}$  and  $\text{V}_\text{O}$ -related normalized defect intensities as expected. Interestingly, these defect intensities appear highest for STO on STO growth, regardless of growth temperature, suggesting some more complex lattice interaction. Thus, Fig. 3(c) illustrates a clear 35 meV upward energy shift of the 1.565 eV  $\text{Ti}^{3+}$  feature with compressive-to-tensile strain [smaller but also apparent in Fig. 3(d)] that may indicate an energy shift of this defect within the  $\text{SrTiO}_3$  bandgap and the relative  $\text{V}_\text{O}$  versus  $\text{Ti}^{3+}$  formation energies.

DRCLS measures strain effects on defect densities in other complex oxides as well. Figure 4 shows DRCL spectra for  $\text{Ba}_{0.5}\text{Sr}_{0.5}\text{TiO}_3$  grown by PLD on (a)  $\text{MgO}(100)$  oriented versus 1% W  $\text{Ba}_{0.5}\text{Sr}_{0.5}\text{TiO}_3$  randomly oriented on  $\text{MgO}(100)$ . Here, the oriented  $\text{Ba}_{0.5}\text{Sr}_{0.5}\text{TiO}_3$  displays high defect intensities relative to the 3.27 eV bandgap feature. Consistent with its  $\text{TiO}_6$  octahedra, its  $\text{O}^{2-}$  2p-derived valence band and  $\text{Ti}^{3+}$   $t_{2g}$ -derived lowest conduction band, this  $(\text{Ba,Sr})\text{TiO}_3$  compound exhibits 1.6, 2.06, and 2.54 eV features similar to those shown for  $\text{SrTiO}_3$  defects in Figs. 1 and 2. Consistent also with the high defect density of Fig. 4(a), this  $(\text{Ba,Sr})\text{TiO}_3$  exhibits high RF dielectric loss of  $\tan \delta = 1.9 \times 10^{-2}$ . In contrast, the much lower defect densities compared to bandgap emission in the spectra of Fig. 4(b) are consistent with this  $(\text{Ba,Sr})\text{TiO}_3$

**TABLE II.** Figure 2 reduction of  $\text{Sr}_{1.2}\text{TiO}_3$  subbandgap 2.0 and 2.6 eV defect emissions by high-temperature oxygen anneal. Pre- and postanneal values shown for both defects are normalized by 3.27 eV NBE values. Reduced values are pre- vs post ratios for each defect.

Depth (nm)	2.0 eV Preanneal	2.0 eV Postanneal	$\Delta 2.0\times$ reduced	2.6 eV Preanneal	2.6 eV Postanneal	$\Delta 2.6\times$ reduced
20	12.9	2.4	5.3	4.2	1.2	3.5
45	20.4	5.1	4.0	6.6	1.8	3.8
85	23.2	11.0	2.1	7.4	3.3	2.3

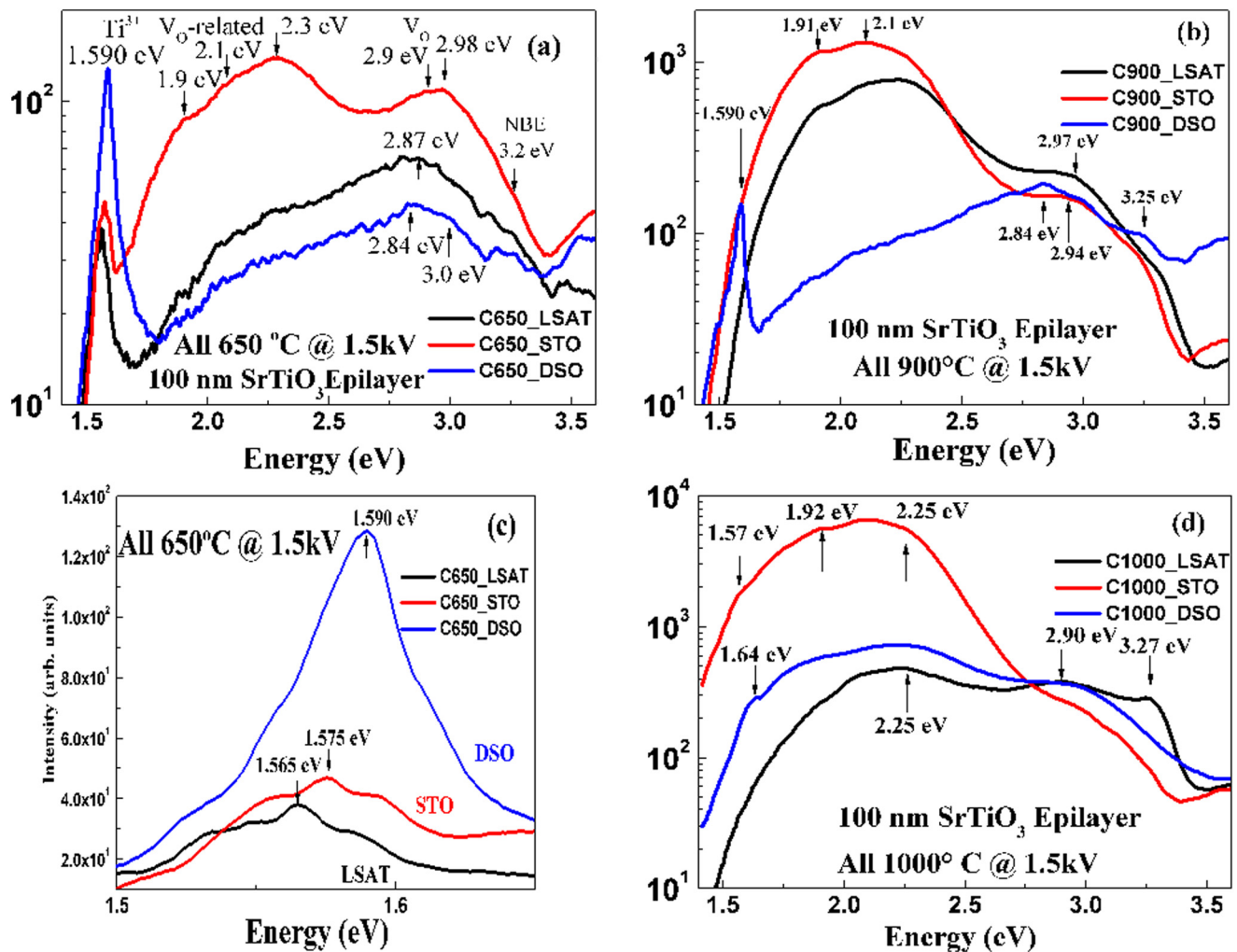


**FIG. 3.** DRCL spectra of 100 nm SrTiO<sub>3</sub> epilayers grown on LSAT, STO, and DSO at temperatures of (a) 650, (b) 900, and (d) 1000 °C, showing orders-of-magnitude changes in defect intensities. In (c), Ti<sup>3+</sup>-related emission peak energy from (a) increases with increasing tensile strain. Each colored spectrum corresponds to the substrate indicated.

compound's  $>2\times$  lower  $\tan \delta = 7.3 \times 10^{-3}$ . The additional 1.76/1.83 eV peaks in these spectra can be identified with  $V_{Ba}$  defects, to be discussed below. The 2.8 eV peak identified as a self-trapped exciton is Fig. 4(b) may be obscured in Fig. 4(a) by the strong defect emission. Figure 4 provides an example of defect densities having a significant effect on electronic properties.<sup>43,44</sup> These results in general provide evidence for the effect of epitaxial strain on defect densities in complex oxides.

With the association of optical transitions in SrTiO<sub>3</sub> and (Ba,Sr)TiO<sub>3</sub> with specific defects, SPS studies can provide energy levels associated with specific transitions within the semiconductor bandgap. Figure 5 insets illustrate photostimulated gap state depopulation and population, respectively. Figure 5(a) shows how contact potential difference  $\Delta cpd$  between the BaTiO<sub>3</sub> free surface and the

Kelvin probe tip exhibits changes in slope with increasing photon energy. Positive slope changes correspond to photostimulated decreases in band bending due to the removal of negative charge from the n-type semiconductor surface. The onset of these transitions occurs at energies below the conduction band as illustrated schematically in Fig. 5(b). Negative slope changes correspond to photostimulated increases in band bending due to the addition of negative charge to the free surface. These transitions appear at energies relative to the valence band. The large increase in cpd between 3.1 and 3.45 eV indicates band flattening due to valence-to-conduction band excitation that increases free electron and hole production.

Figure 5(b) shows that these transitions can all be matched as complementary pairs whose approximate sum adds up to the 3.1 eV

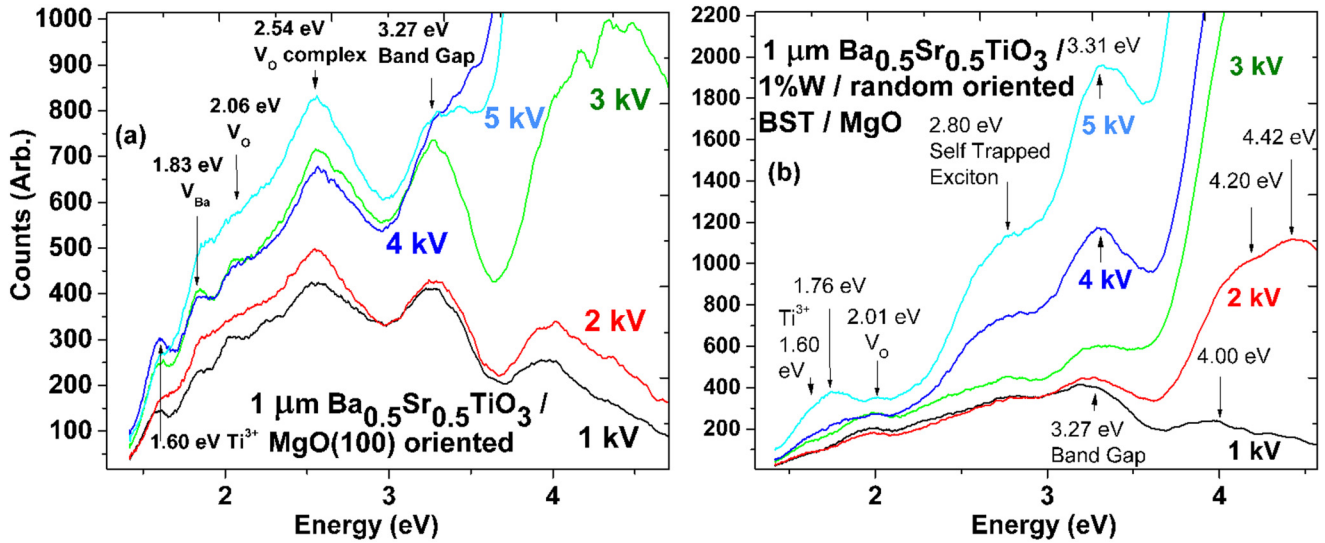


FIG. 4. DRCL spectra of PLD-grown  $\text{Ba}_{0.5}\text{Sr}_{0.5}\text{TiO}_3$  (a) on MgO (100)-oriented and (b) on 1%W  $\text{Ba}_{0.5}\text{Sr}_{0.5}\text{TiO}_3$  randomly oriented on MgO. Each colored spectrum corresponds to an incident beam energy  $E_B$  in kV and its corresponding maximum excitation depth  $R_B$  in nm as indicated.

$\text{BaTiO}_3$  bandgap. (Note: the 0.7 eV complement to the 2.4 eV transition is outside the spectral range.) The  $\text{TiO}_6$  octahedral correspondence between  $\text{BaTiO}_3$ ,  $\text{SrTiO}_3$ , and  $(\text{Ba,Sr})\text{TiO}_3$  mentioned above suggests that approximately the same energies correspond to analogous defects in all three materials. Thus, the 1.60/1.75 eV pair can be

associated with  $\text{Ti}^{3+}$ -related states, while the 1.952/2.1 eV pair can be associated with  $\text{V}_O$ -related states. The 2.9 eV transition that appears in both DRCLS and SPS may also correspond to  $\text{V}_O$ -related ( $\text{V}_O\text{-R}$ ) states based on its sensitivity to oxygen anneals shown in Fig. 2 and to growth temperature in Fig. 3.

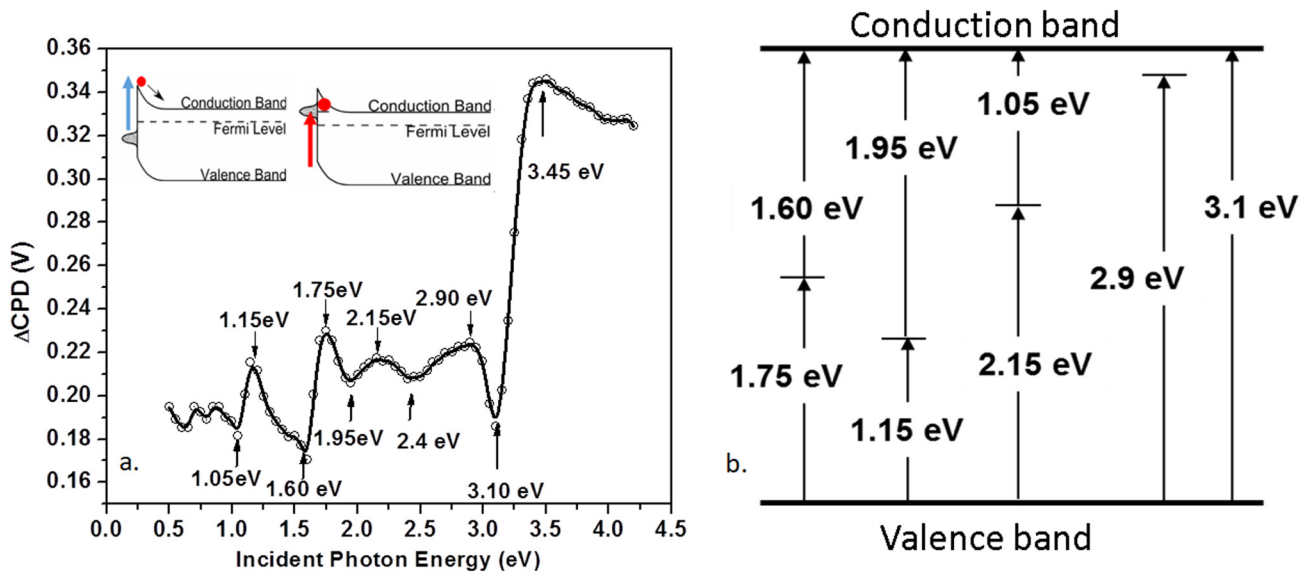


FIG. 5. (a) Schematic illustration of  $\text{BaTiO}_3$  photostimulated charge carrier depopulation (upper left) out of and population (upper right) of charge carriers into defect energy levels within the bandgap. Depopulation (population) transitions correspond to positive (negative) SPS cpd slope changes with increasing photon energy. (b) Schematic energy level diagram illustrating these transitions.

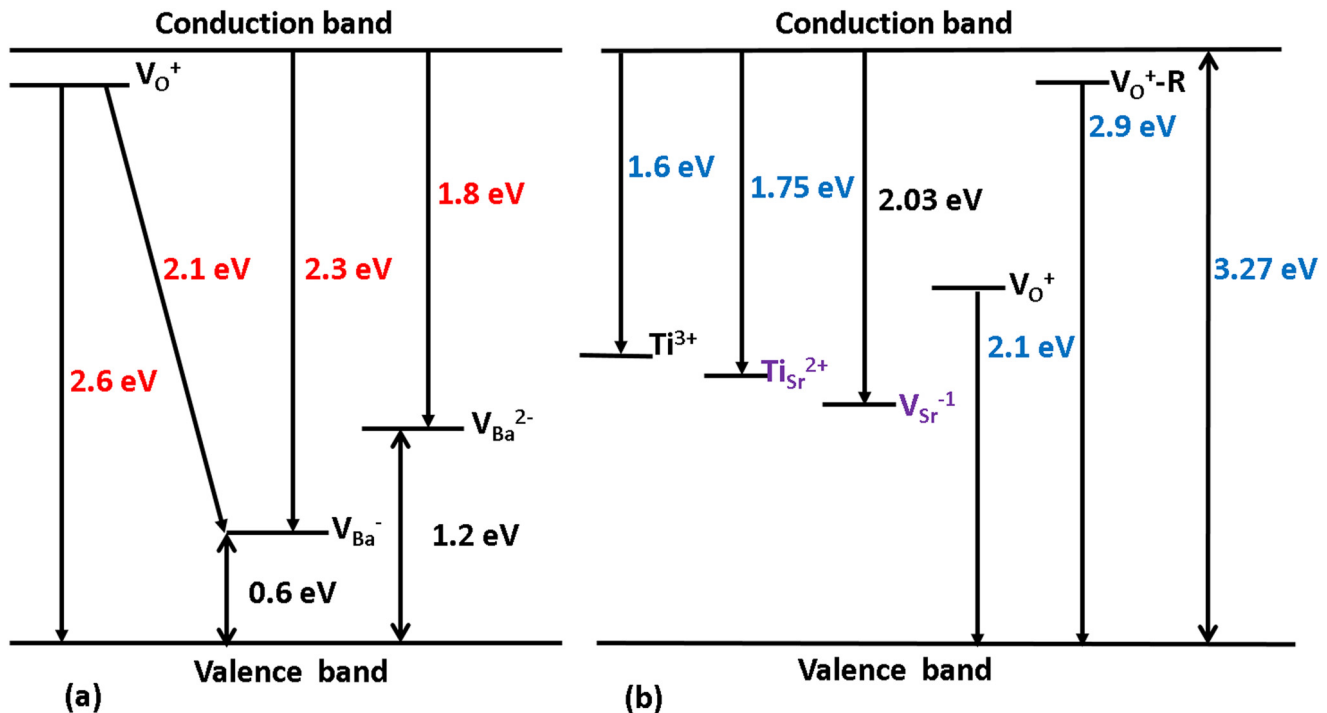


FIG. 6. BaTiO<sub>3</sub> schematic energy level diagram (a) with downward arrow transitions after Koschek and Kubalek (Ref. 60). Reprinted with permission from Koschek and Kubalek, Phys. Stat. Solidi A 79, 131 (1983). Copyright 1983, John Wiley & Sons. (b) Downward arrow transitions suggested by Figs. 1–3 and 5.

Both 2.9 and 1.95/1.15 eV pair SPS features can be related to specific defects based on CL measurements of sintered BaTiO<sub>3</sub> grains and theory of Koschek and Kubalek<sup>60</sup> as reproduced in Fig. 6(a) based on earlier conductivity measurement-derived defect activation energies of Daniels and Hårdtl.<sup>61</sup> The proximity of Fig. 5(d)'s 1.95/1.15 eV pair to the 1.8/1.2 eV pair shown in Fig. 6(a) suggests their association with V<sub>Ba</sub><sup>2-</sup> defect transitions in Fig. 6(a). The Ba<sub>0.5</sub>Sr<sub>0.5</sub>TiO<sub>3</sub> DRCL spectra in Fig. 4(a) indeed display a clear transition at 1.83 eV that can be related to this defect.

Based on Figs. 5(b) and 6(a), Fig. 6(b) suggests optical transitions into and out of energy levels within the BaTiO<sub>3</sub> bandgap. The 1.6 eV transition corresponds to an energy level of 1.6 eV below conduction band E<sub>C</sub> and can be identified with Ti<sup>3+</sup> states as discussed earlier.

Recent studies involving iterative feedback among atomic-layer-and stoichiometry-controlled thin-film epitaxy, hybrid density function theory, and high depth-resolution CL spectroscopy identified a functional cationic defect, the Ti antisite (Ti<sub>Sr</sub>) defect with an energy of 1.74 eV.<sup>62</sup> This work also attributed a 2.03 eV emission to V<sub>Sr</sub><sup>-1</sup>. However, previous work<sup>26</sup> showed low 2 eV emission for Sr<sub>0.8</sub>TiO<sub>3</sub>, increasing with increasing Sr content for SrTiO<sub>3</sub> and Sr<sub>1.2</sub>TiO<sub>3</sub>, suggesting a stronger contribution from V<sub>O</sub><sup>+</sup> defects as suggested by Figs. 1–3. The 2.1 eV transition in Fig. 6(a) also suggests that transitions between V<sub>O</sub><sup>+</sup>-V<sub>Ba</sub><sup>-</sup> donor-acceptor pairs can contribute to defect luminescence.

#### IV. CRYSTAL ORIENTATION AND ELECTRIC FIELD EFFECTS ON SrTiO<sub>3</sub> INTRINSIC POINT DEFECTS

DRCLS results show how both complex oxide crystal orientation and applied electric fields can redistribute intrinsic point defects in complex oxides. Based on defect identifications of characteristic optical emissions obtained in Sec. III, DRCL spectra of bulk SrTiO<sub>3</sub> crystals exhibit dominant emissions at 1.62 eV corresponding to Ti<sup>3+</sup> defects and 1.9–2.0 eV corresponding to V<sub>O</sub> defects. The strength of these defect emissions varies strongly with depth from the free surface on a scale of tens of nanometers. Furthermore, these depth distributions vary significantly with crystal surface orientation.

Figure 7(a) shows Ti<sup>3+</sup> and V<sub>O</sub> normalized depth distributions I(defect)/I(NBE) for SrTiO<sub>3</sub>(111). Here, 2.0 eV V<sub>O</sub> CL intensity decreases steadily from bulk depths greater than 100 nm to less than a few nanometers of the free surface. The 1.62 eV Ti<sup>3+</sup> emission intensity also decreases steadily from the bulk but then increases rapidly within ~10 nm of the surface. As a result, the ratio of Ti<sup>3+</sup> to V<sub>O</sub> intensities increases by nearly 3× from approximately unity in the bulk to the surface. The near-surface defect distributions are significantly different for (110) and (100) orientations. Figure 7(b) shows that V<sub>O</sub> intensities are nearly an order of magnitude higher than Ti<sup>3+</sup> intensities at all depths but exhibit a steep decline within the outermost 10 nm to only I(2.0 eV)/I(1.6 eV) of only ~2× V<sub>O</sub>-rich. Figure 7(c) shows a

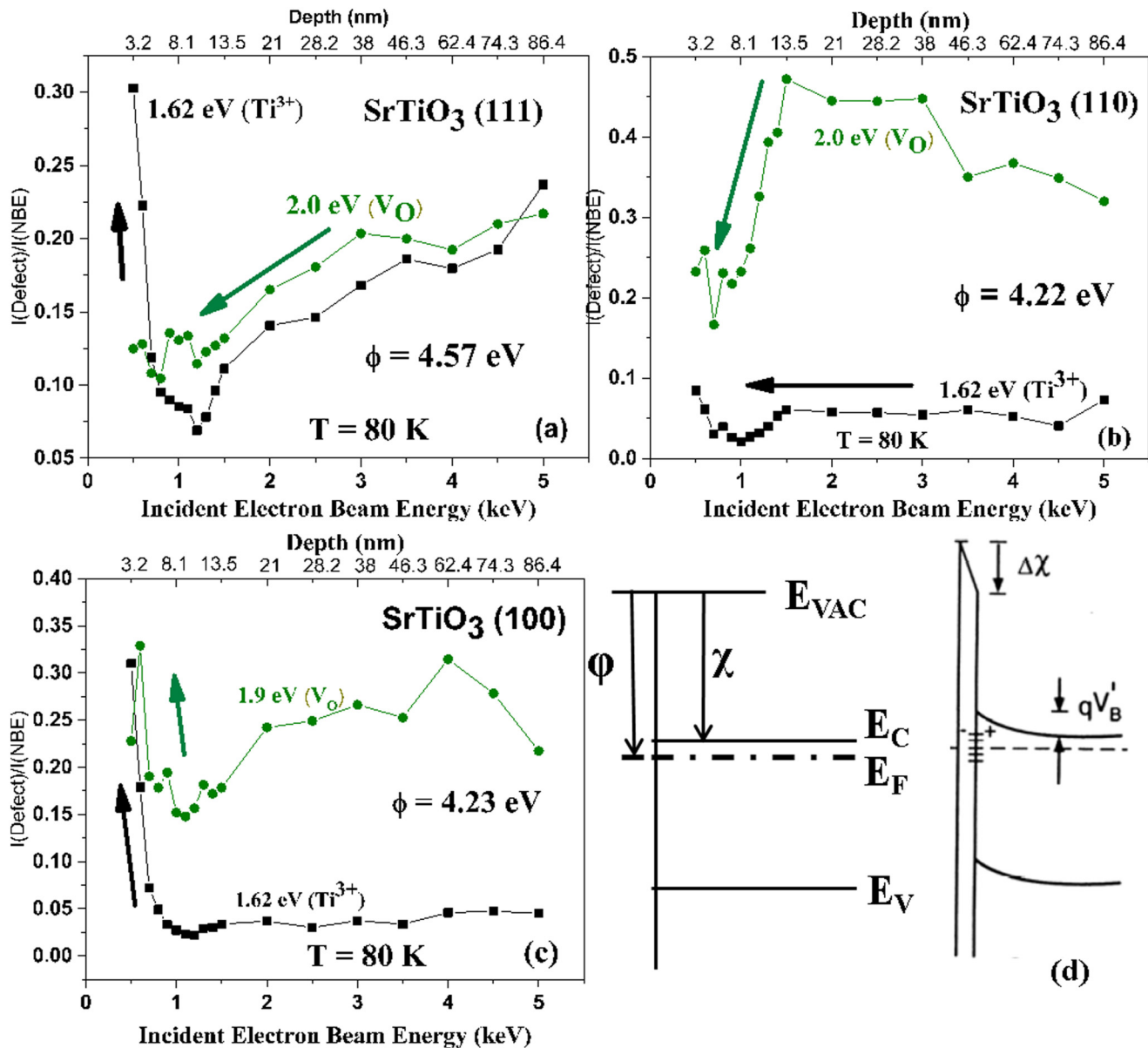
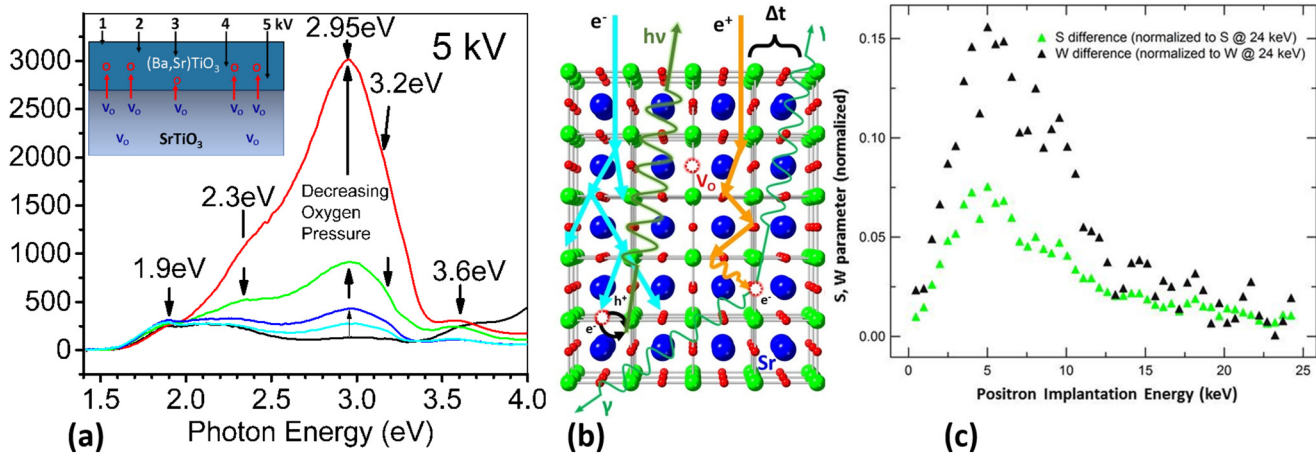


FIG. 7. DRCLS—measured depth distributions at 80 K of bulk SrTiO<sub>3</sub> Ti<sup>3+</sup> and V<sub>O</sub> defects for (a) (111), (b) (110), and (c) 100 orientations. KPFM-measured work functions  $\phi$  shown are highest for SrTiO<sub>3</sub>(111). Colored depth profiles correspond to V<sub>O</sub> and Ti<sup>3+</sup> intrinsic defects as indicated. Schematic diagrams in (d) define surface work function  $\phi$ , electron affinity  $\chi$ , and surface dipole  $\Delta\chi$ .

similar V<sub>O</sub>-rich distribution to within ~10 nm of the free surface but then nearly equal  $I(2.0 \text{ eV})$  and  $I(1.6 \text{ eV})$  intensities within the last few nanometers.

KPFM measurements of these different surface orientations showed significant differences in their absolute surface potential. The Kelvin probe used for these measurements was calibrated immediately beforehand with an air-stable, freshly cleaved, highly oriented, polycrystalline graphite surface.<sup>63</sup> Surface potentials  $\phi$

were 4.57, 4.22, and 4.23 eV for (111), (110), and (100) surface orientations, respectively. Interestingly, for Nb-doped SrTiO<sub>3</sub> (not shown),  $\phi$  is 3.59 eV, i.e., with its Fermi level 0.6 eV higher than for the lowest work function for nominally undoped SrTiO<sub>3</sub> and consistent with its n-type, degenerate doping and Fermi level above its conduction band minimum versus inside the band gap without extrinsic doping. The 0.35 eV larger surface work function for the Ti<sup>3+</sup>-rich (111) versus the more  $I(\text{Ti}^{3+})/I(\text{V}_\text{O})$ -balanced (110) and



**FIG. 8.** (a)  $E_B = 5$  kV  $\text{Ba}_{0.5}\text{Sr}_{0.5}\text{TiO}_3$  DRCLS. 2.95 eV emission increases with decreasing plasma-assisted  $\text{O}_2$  growth pressure (Ref. 42). Each colored spectrum corresponds to a different oxygen growth pressure, decreasing as the arrows indicate. (b) Comparison of DRCLS and PAS depth dependence based on their scattering, electron-hole recombination, light emission (DRCLS), and incident vs exiting x-ray time delay (PAS). (c) PAS S,W parameters vs positron implantation energy exhibiting maxima at 5 keV (Ref. 42). Reprinted with permission from Rutkowski *et al.*, J. Phys. D: Appl. Phys. **47**, 255303 (2014). Copyright 2014, IOP Publishing.

(100) surface orientations corresponds to a difference in surface dipole  $\Delta\chi$  as shown in Fig. 7(d). This  $\Delta\chi$  represents a voltage  $V$  defined by capacitance  $C = Q/V = \epsilon A/d$ , where  $\epsilon/\epsilon_0 = 300$  nominally for  $\text{SrTiO}_3$ ,  $d$  is charge separation,  $A$  is the surface area, charge  $Q = qn_s$  is the surface charge, and  $n_s$  is the surface charge density. Hence,  $n_s = \epsilon A \Delta\chi/qd = 5.8 \times 10^{13}$  electrons  $\text{cm}^{-2}$ . For  $\text{SrTiO}_3$  with lattice constant  $a_0 = 3.905$  Å and surface atomic density  $1/a_0^2 = 6.55 \times 10^{14}$   $\text{cm}^{-2}$ , then  $n_s = 8.9$  electrons per 100 surface atoms, equivalent to a volume charge density of  $\sim 4 \times 10^{20}$   $\text{cm}^{-3}$  within the outer 10 nm depth. Hence, there is a massive defect segregation with defects attributed to  $\text{Ti}^{3+}$  and  $\text{V}_O$  tracking independently between orientations. Their opposite redistribution between (111) and (110) or (100) orientations contribute to significant surface dipoles. Photoemission spectroscopy studies of MBE-grown  $\text{BaTiO}_3/\text{SrTiO}_3$  heterojunctions report even larger dipoles.<sup>64</sup> The dramatic depletion of  $\text{V}_O$  within the outer  $\sim 10$  nm depth of the  $\text{SrTiO}_3$  surface was also observed in electric field-induced  $\text{V}_O$  migration studies<sup>65</sup> and is consistent with theoretical predictions.<sup>66</sup> Note that these KPFM measurements were performed in the dark and in air, independent of any extrinsic defects introduced by nonstoichiometry, chemical treatments, or other processing.<sup>67,68</sup>

Previous studies of complex oxide surface polarity<sup>69</sup> considered II–IV perovskites such as  $\text{SrTiO}_3$  with surface crystallographic orientations that are described according to Tasker notation<sup>70</sup> as type I Polar with  $\text{SrO}$  or  $\text{TiO}_2$  surface termination for cubic (100) orientation or type III Polar with  $\text{O}_2$  or  $\text{BaTiO}$  surface termination for cubic (110) orientation or  $\text{SrO}_3$  or  $\text{Ti}$  termination for cubic (111) orientation. Type I surfaces consist of a stack of neutral ionic planes. Type III surfaces consist of a stack of charge ionic planes that produce a net dipole. Significantly, the defect distribution plotted in Fig. 7(c) for the (100) surface orientation termed type I shows relatively equal intensities for the 1.9–2 eV  $\text{V}_O$  and 1.62 eV

$\text{Ti}^{3+}$  defects, whereas the defect distribution plotted in Fig. 7(b) for the (110) surface orientation termed type III and the defect distribution plotted in Fig. 7(a) for the (111) surface orientation also termed type III display asymmetric defect distributions—higher  $\text{V}_O$  intensities for the (110) orientation versus higher  $\text{Ti}^{3+}$  for the (111) orientation. Correspondingly, the (110) orientation has work function of  $\Delta\Phi = 4.22$  eV, whereas the (111) orientation has work function of  $\Delta\Phi = 4.57$  eV. The higher work function corresponds to a more negative (111) surface, consistent with the higher  $\text{Ti}^{3+}$  versus  $\text{V}_O$  near-surface ionic density. Thus, the near-surface defect distribution and work function differences versus crystal orientation can be viewed as either an electrostatic or a thermodynamic<sup>66</sup> effect.

## V. ELECTRONIC EFFECTS OF COMPLEX OXIDE DEFECTS

Defects in complex oxides can strongly affect properties of electronic device structures—not only because of their deep level nature than can act as electrically compensating, tunneling, or recombination centers but because such defects in widely used materials such as  $\text{SrTiO}_3$  or  $\text{BaTiO}_3$  can diffuse under applied electric fields. The unique interface properties of these materials are particularly challenging since defects can form at or segregate to such junctions unless growth and processing conditions are well controlled.

One such example is  $\text{Ba}_{0.5}\text{Sr}_{0.5}\text{TiO}_3$  grown on  $\text{SrTiO}_3$  by MBE. DRCLS shows that oxygen vacancies form at their interface as the growing  $\text{Ba}_{0.5}\text{Sr}_{0.5}\text{TiO}_3$  epilayer extracts O from the underlying substrate. Figure 8(a) illustrates this process schematically. DRCL spectral features include the  $\text{V}_O$ -R feature at 2.9 eV whose intensity depends strongly on  $\text{O}_2$  pressure during the epilayer growth. With decreasing  $\text{O}_2$  pressure, this feature increases by an order of magnitude as the  $\text{Ba}_{0.5}\text{Sr}_{0.5}\text{TiO}_3$  epilayer grows.<sup>42</sup> DRCLS

shows that this defect grows primarily in the SrTiO<sub>3</sub> at the interface with Ba<sub>0.5</sub>Sr<sub>0.5</sub>TiO<sub>3</sub>. Positron annihilation spectroscopy (PAS) confirms the depth location of this V<sub>O</sub>-R growth in Fig. 8(c). PAS also provides semiquantitative defect densities, here estimated at >10<sup>18</sup> cm<sup>-3</sup>. Such high densities are consistent with the dipole charge density described in Fig. 7. Figure 8(b) shows that DRCLS and PAS are natural complements since the depth dependences of incident electrons and positrons are the same.<sup>71</sup> The extraction of substrate oxygen by growing oxide overlayers is well known from much earlier studies of high-temperature superconductors such as YBa<sub>2</sub>Cu<sub>3</sub>O<sub>7-δ</sub> and other high-temperature superconductors<sup>72</sup> as well as LaAlO<sub>3</sub> and TiO<sub>3</sub>.<sup>73</sup> Such oxygen outdiffusion is enabled by oxygen's O<sup>3+</sup>/O<sup>4+</sup> multiple charge states.

BaTiO<sub>3</sub> is a promising candidate for electrooptic and GHz RF devices due to its high tunable and anisotropic dielectric permittivity.<sup>74</sup> Yet its dielectric loss can be limited by the presence of intrinsic point defects. Nevertheless, extended air anneals at high temperature to reduce oxygen vacancies and other defects dramatically improve its RF performance at GHz frequencies.<sup>75</sup>

The movement of V<sub>O</sub> under applied electric fields inside SrTiO<sub>3</sub> is a significant concern for its use for high-voltage capacitors since these defects can move macroscopic distances,<sup>67</sup> forming conductive pathways and potentially contributing to dielectric breakdown.<sup>65,67</sup>

Perhaps the most striking example of a defect contribution to interface effects has been for the LaAlO<sub>3</sub>/SrTiO<sub>3</sub> interface. Here the control of oxygen vacancies by growth techniques has led to the observation of 2DHG. By strongly reducing oxygen vacancies in the SrTiO<sub>3</sub> epilayer on LaAlO<sub>3</sub>, researchers could prevent the compensation of holes that would otherwise give rise to the formation of a two-dimensional hole gas (2DHG).<sup>76</sup> This advance was recognized as enabling entirely new functionality in complex oxides by formation of dual 2DHG-2DEG structures.<sup>77</sup> Other complex oxide interfaces such as LaNiO<sub>3</sub>/La<sub>2/3</sub>Sr<sub>1/3</sub>MnO<sub>3</sub>/SrTiO<sub>3</sub> heterostructures also exhibit unique interface-specific features that DRCLS could identify on a nanometer scale.<sup>78</sup>

## VI. CONCLUSIONS—NEW DIRECTIONS

The direct measurement and understanding of intrinsic point defects in complex oxides can further advance by combining DRCLS with other advanced characterization techniques. Figure 8 shows how DRCLS combined with PAS provides not only confirmation of interface-specific defect features but also calibrations (in Fig. 8, only a lower limit) of their defect densities. Positron annihilation spectroscopy can provide analogous information for complex oxides such as SrTiO<sub>3</sub>.<sup>79</sup> The combination of DRCLS with SPS shown here provides new information about the energy levels of depth-dependent defect densities as shown in Fig. 5. DRCLS combined with temperature-dependent Hall (TDH) measurements can correlate specific defects with donor and acceptor formation and their contribution to electrical properties.<sup>80</sup> X-ray photoemission spectroscopy can define stoichiometries that correlate with specific defect emissions and their physical nature, for example, a nitrogen vacancy that acts as an ScN impurity and oxygen doping precursor.<sup>49</sup> Photo-EPR can provide energy level as well as spin-descriptive defect information.<sup>53</sup> Impedance spectroscopy is yet

another powerful tool for describing the electric transport properties of intrinsic point defects, particularly when combined with DRCLS in three dimensions.<sup>65</sup> Finally, DRCLS combined with scanning TEM/electron energy loss spectroscopy line profiles provide powerful analytic techniques at the atomic scale that can reveal atomic composition and bonding configurations.<sup>81</sup>

Overall, the results presented here show that the DRCLS and SPS techniques together can provide a powerful set of electronic, spatial, growth, and processing tools for detecting and characterizing intrinsic point defects in SrTiO<sub>3</sub>, BaTiO<sub>3</sub>, and other complex oxides. The combination of DRCLS with SPS with other advanced characterization techniques will further expand the understanding of these complex oxide defects and could lead not only to their physical control but also to new electronic device designs.

## ACKNOWLEDGMENTS

L.J.B., J.Z., K.M., S.B., and Z.Q.Z. gratefully acknowledge support for this work by the National Science Foundation (NSF) Grant No. DMR-18-00130 (Tanya Paskova). The authors thank Lisa Alldredge, Wontae Chang, and Steven Kirchoefer at NRL for providing the (Ba,Sr)TiO<sub>3</sub> samples discussed here.

## DATA AVAILABILITY

The data that support the findings of this study are available from the corresponding author upon reasonable request.

## REFERENCES

- A. Ohtomo and H. Y. Hwang, *Nature* **427**, 423 (2004).
- S. Thiel, G. Hammerl, A. Schmehl, C. W. Schneider, and J. Mannhart, *Science* **313**, 1942 (2006).
- M. Takizawa *et al.*, *Phys. Rev. Lett.* **97**, 057601 (2006).
- N. Nakagawa, H. Y. Hwang, and D. A. Muller, *Nat. Mater.* **5**, 204 (2006).
- M. Huijben, G. Rijnders, D. H. A. Blank, S. Bals, S. Van Aert, J. Verbeeck, G. Van Tendeloo, A. Brinkman, and H. Hilgenkamp, *Nat. Mater.* **5**, 556 (2006).
- W. Siemons, G. Koster, H. Yamamoto, W. A. Harrison, T. H. Geballe, D. H. A. Blank, and M. R. Beasley, *Phys. Rev. Lett.* **98**, 196802 (2007).
- S. A. Chambers, *Surf. Sci. Rep.* **39**, 105 (2000).
- S. A. Chambers *et al.*, *Surf. Sci. Rep.* **65**, 317 (2010).
- L. Qiao, T. C. Droubay, T. Varga, M. E. Bowden, V. Shutthanandan, Z. Zhu, T. C. Kaspar, and S. A. Chambers, *Phys. Rev. B* **83**, 085408 (2011).
- S. A. Chambers, Y. Liang, Z. Yu, R. Droopad, and J. Ramdani, *J. Vac. Sci. Technol. A* **19**, 934 (2001).
- L. J. Brillson, *Phys. Rev. Lett.* **40**, 260 (1978).
- L. J. Brillson, *Phys. Rev.* **18**, 2431 (1978).
- S. A. Chambers, *Adv. Mater.* **22**, 219 (2010).
- L. J. Brillson, *J. Phys. D: Appl. Phys.* **45**, 183001 (2012).
- L. J. Brillson, H. W. Richter, M. L. Slade, B. A. Weinstein, and Y. Shapira, *J. Vac. Sci. Technol. A* **3**, 1011 (1985).
- L. J. Brillson, *J. Vac. Sci. Technol. B* **19**, 1762 (2001).
- H. C. Gatos and J. Lagowski, *J. Vac. Sci. Technol.* **10**, 130 (1973).
- J. Lagowski, C. L. Balestra, and H. C. Gatos, *Surf. Sci.* **29**, 203 (1972).
- L. J. Brillson, *J. Vac. Sci. Technol.* **12**, 249 (1975).
- B. G. Yacobi and D. B. Holt, *Cathodoluminescence Microscopy of Inorganic Solids* (Plenum, New York, 1990).
- C. B. Norris, C. E. Barnes, and W. Beezhold, *J. Appl. Phys.* **44**, 3209 (1973).
- L. J. Brillson, C. F. Brucker, A. D. Katnani, N. G. Stoffel, and G. Margaritondo, *Appl. Phys. Lett.* **38**, 784 (1981).
- L. J. Brillson, *J. Vac. Sci. Technol.* **20**, 652 (1982).

- <sup>24</sup>R. E. Viturro, M. L. Slade, and L. J. Brillson, *Phys. Rev. Lett.* **57**, 487 (1986).
- <sup>25</sup>H. L. Mosbacker, Y. M. Strzhemechny, B. D. White, P. E. Smith, D. C. Look, D. C. Reynolds, C. W. Litton, and L. J. Brillson, *Appl. Phys. Lett.* **87**, 012102 (2005).
- <sup>26</sup>L. J. Brillson and Y. Lu, *J. Appl. Phys.* **109**, 121301 (2011).
- <sup>27</sup>J. Zhang, S. Walsh, C. Brooks, D. G. Schlom, and L. J. Brillson, *J. Vac. Sci. Technol. B* **26**, 1466 (2008).
- <sup>28</sup>A. J. Hauser, J. Zhang, L. Mier, R. A. Ricciardo, P. M. Woodward, T. L. Gustafson, L. J. Brillson, and F. Y. Yang, *Appl. Phys. Lett.* **92**, 222901 (2008).
- <sup>29</sup>J. Zhang, M. Rutkowski, L. W. Martin, T. Conry, R. Ramesh, J. F. Ihlefeld, A. Melville, D. G. Schlom, and L. J. Brillson, *J. Vac. Sci. Technol. B* **27**, 2012 (2009).
- <sup>30</sup>J. Zhang, D. Doust, J. Chakhalian, M. Kareev, J. Liu, S. Prosandeev, and L. J. Brillson, *Appl. Phys. Lett.* **94**, 092904 (2009).
- <sup>31</sup>Shaoping Shen, Yiqun Liu, R. G. Gordon, and L. J. Brillson, *Appl. Phys. Lett.* **98**, 172902 (2011).
- <sup>32</sup>T. H. Kim *et al.*, *Phys. Rev. B* **101**, 121105(R) (2020).
- <sup>33</sup>C.-H. Lin, T. A. Merz, D. R. Doust, J. Joh, J. A. Del Alamo, U. K. Mishra, and L. J. Brillson, *IEEE Trans. Electron. Dev.* **59**, 2667 (2012).
- <sup>34</sup>A. Rose, *RCA Rev.* **27**, 600 (1966).
- <sup>35</sup>P. Hovington, D. Drouin, and R. Gauvin, *Scanning* **19**, 1 (1997).
- <sup>36</sup>D. Drouin, A. R. Couture, D. Joly, X. Tastet, V. Aimez, and R. Gauvin, *Scanning* **29**, 92 (2007).
- <sup>37</sup>C. A. Klein, *J. Appl. Phys.* **39**, 2029 (1968).
- <sup>38</sup>M. P. Seah and W. A. Dench, *Surf. Int. Anal.* **1**, 2 (1979).
- <sup>39</sup>T. E. Everhart and P. H. Hoff, *J. Appl. Phys.* **42**, 5837 (1971).
- <sup>40</sup>L. J. Brillson, in *Surface and Interfaces of Electronic Materials* (Wiley-VCH, Weinheim, 2010), Chap. 16.
- <sup>41</sup>M. Kareev, S. Prosandeev, J. Liu, C. Gan, A. Kareev, J. W. Freeland, M. Xiao, and J. Chakhalian, *Appl. Phys. Lett.* **93**, 061909 (2008).
- <sup>42</sup>M. M. Rutkowski, K. McNicholas, Z. Q. Zeng, F. Tuomisto, and L. J. Brillson, *J. Phys. D: Appl. Phys.* **47**, 255303 (2014).
- <sup>43</sup>L. M. B. Alldredge, W. Chang, S. B. Qadri, S. W. Kirchoefer, and J. M. Pond, *Appl. Phys. Lett.* **90**, 212901 (2007).
- <sup>44</sup>M. E. Twigg, L. M. B. Alldredge, W. Chang, A. Podpirka, S. W. Kirchoefer, and J. M. Pond, *Thin Solid Films* **548**, 178 (2015).
- <sup>45</sup>W. Chang, L. M. Alldredge, S. W. Kirchoefer, and J. M. Pond, *J. Appl. Phys.* **102**, 014105 (2007).
- <sup>46</sup>H. Bethe, *Ann. Phys.* **5**, 325 (1930).
- <sup>47</sup>K. van Benthem, C. Elsässer, and R. H. French, *J. Appl. Phys.* **90**, 6156 (2001).
- <sup>48</sup>M. Walker, A. Jarry, N. Pronin, J. Ballard, G. Rubloff, and L. J. Brillson, *J. Mater. Chem. A* **8**, 11800 (2020).
- <sup>49</sup>M. S. Haseman, B. A. Noesges, S. Shields, J. S. Cetnar, A. N. Reed, H. A. Al-Atabi, J. H. Edgar, and L. J. Brillson, *APL Mater.* **8**, 081103 (2020).
- <sup>50</sup>H. Ihrig, J. H. T. Hengst, and M. Klerk, *Z. Phys. B: Condens Matter* **16**, S261 (2004).
- <sup>51</sup>A. K. Ghosh, F. G. Wakim, and R. R. Addiss, Jr., *Phys. Rev.* **184**, 979 (1969) and references therein.
- <sup>52</sup>R. Plugaru, A. Cremades, and J. Piqueras, *J. Phys.: Condens. Matter* **16**, S261 (2003).
- <sup>53</sup>S. Yang, L. E. Halliburton, A. Manivannan, P. H. Bunton, D. B. Baker, M. Klemm, S. Horn, and A. Fujishima, *Appl. Phys. Lett.* **94**, 162114 (2009).
- <sup>54</sup>D. Maestre, A. Cremades, and J. Piqueras, *Nanotechnology* **17**, 1584 (2006).
- <sup>55</sup>R. Sanjinés, H. Tang, H. Berger, F. Gozzo, G. Margaritondo, and F. Lévy, *J. Appl. Phys.* **75**, 2945 (1994).
- <sup>56</sup>J.-M. Wu, H. C. Shih, W.-T. Wu, Y.-K. Tseng, and I.-C. Chen, *J. Cryst. Growth* **281**, 384 (2005).
- <sup>57</sup>F. J. Morin and J. R. Oliver, *Phys. Rev. B* **8**, 5847 (1973).
- <sup>58</sup>J. Dashdorj, M. Zvanut, and L. J. Stanley, *J. Appl. Phys.* **107**, 083513 (2010).
- <sup>59</sup>S. Shibagaki, A. Hamano, S. Takao, and J. Tanaka, *J. Ceram. Soc. Jpn.* **102**, 858 (1994).
- <sup>60</sup>G. Koschek and E. Kubalek, *Phys. Stat. Solidi A* **79**, 131 (1983).
- <sup>61</sup>J. Daniels and K. H. Härdtl, *Philips Res. Rep.* **81**, 489 (1976).
- <sup>62</sup>D. Lee, H. Wang, B. A. Noesges, T. Asel, J. Pan, Q. Yan, L. Brillson, X. Wu, and C.-B. Eom, *Phys. Rev. Mater.* **2**, 060403(R) (2018).
- <sup>63</sup>W. N. Hansen and G. J. Hansen, *Surf. Sci.* **481**, 172 (2001).
- <sup>64</sup>S. Balaz, Z. Zeng, and L. J. Brillson, *J. Appl. Phys.* **114**, 183701 (2013).
- <sup>65</sup>H. Gao, S. Sahu, C. Randall, and L. J. Brillson, *J. Appl. Phys.* **127**, 094105 (2020).
- <sup>66</sup>R. A. De Souza, V. Metlenko, D. Park, and T. E. Weirich, *Phys. Rev. B* **85**, 174109 (2012).
- <sup>67</sup>M. S. J. Marshall, A. E. Becerra-Toledo, L. D. Marks, and M. R. Castell, in *Defects at Oxide Surfaces*, edited by J. Jupille, and G. Thornton (Springer International, New York, 2015), Vol. 58, pp. 327–349.
- <sup>68</sup>S. Cook, M. T. Dylla, R. A. Rosenberg, Z. R. Mansley, G. J. Snyder, L. D. Marks, and D. D. Fong, *Adv. Electron. Mater.* **5**, 1800460 (2019).
- <sup>69</sup>J. Goniakowski, F. Finocchi, and C. Noguera, *Rep. Prog. Phys.* **71**, 016501 (2008).
- <sup>70</sup>P. W. Tasker, *J. Phys. C: Solid State Phys.* **12**, 4977 (1979).
- <sup>71</sup>F. Tuomisto and I. Makkonen, *Rev. Mod. Phys.* **85**, 1583 (2013).
- <sup>72</sup>L. S.-J. Peng, W. Wang, W. Jo, T. Ohnishi, A. F. Marshall, R. H. Hammond, M. R. Beasley, E. J. Peterson, and R. E. Ericson, *IEEE Trans. Appl. Supercond.* **11**, 3375 (2001).
- <sup>73</sup>C. W. Schneider, M. Döbeli, C. Richter, and T. Lippert, *Phys. Rev. Mater.* **3**, 123401 (2019).
- <sup>74</sup>A. Feteira, D. C. Sinclair, I. M. Reaney, Y. Somiya, and M. T. Lanagan, *J. Am. Ceram. Soc.* **87**, 1082 (2004).
- <sup>75</sup>Z. Q. Zeng, A. Podpirka, S. W. Kirchoefer, T. J. Asel, and L. J. Brillson, *Appl. Phys. Lett.* **106**, 182903 (2015).
- <sup>76</sup>H. Lee *et al.*, *Nat. Mater.* **17**, 231 (2018).
- <sup>77</sup>Y. Chen and N. Pryds, *Nat. Mater.* **17**, 215 (2018).
- <sup>78</sup>T. J. Asel, H. Gao, T. J. Heintz, D. Adkins, P. M. Woodward, J. Hoffman, A. Bhattacharya, and L. J. Brillson, *J. Vac. Sci. Technol. B* **33**, 04E103 (2015).
- <sup>79</sup>F. A. Selim, D. Winarski, C. R. Varney, M. C. Tarun, J. Ji, and M. D. McCluskey, *Results Phys.* **5**, 28 (2015).
- <sup>80</sup>H. Gao, S. Muralidharan, M. D. Rezaul Karim, S. M. White, Lei R. Cao, K. M. Leedy, H. Zhao, D. C. Look, and L. J. Brillson, *J. Phys. D: Appl. Phys.* **53**, 465102 (2020).
- <sup>81</sup>D. A. Muller, N. Nakagawa, A. Ohtomo, J. L. Grazul, and H. Y. Hwang, *Nature* **430**, 657 (2004).
- <sup>82</sup>See supplementary material at <https://www.scitation.org/doi/suppl/10.1116/6.0001339> for DRCL spectra of SrTiO<sub>3</sub> Fe impurity peak emissions distinguished from spectra presented here.

**Supplemental Information for “Deep Level Defect Spectroscopies of Complex Oxide Surfaces and Interfaces” by J. Zhang et al., JVA21-AR-SC2021-00386**

J. Zhang<sup>1</sup>, K. McNicholas,<sup>2</sup> S. Balazs<sup>3</sup>, Z.Q. Zeng,<sup>4</sup> D. Schlom<sup>5,6</sup>, and L. J. Brillson<sup>7,8\*</sup>

<sup>1</sup> Spears School of Business, Oklahoma State University, Stillwater, OK 74078 USA

<sup>2</sup> MIT Lincoln Laboratories, Lexington, MA 02421 USA

<sup>3</sup> Department of Physics, Astronomy, Geology, and Environmental Science, Youngstown State University, Youngstown, OH, 44555 USA

<sup>4</sup> II-VI Incorporated, Warren, PA 07059 USA

<sup>5</sup> Department of Materials Science and Engineering, Cornell University, Ithaca, NY 14853, USA

<sup>6</sup> Kavli Institute at Cornell for Nanoscale Science, Ithaca, NY, USA. 14853, USA

<sup>7</sup> Department of Electrical & Computer Engineering, The Ohio State University, Columbus, OH 43210, USA

<sup>8</sup> Department of Physics, The Ohio State University, Columbus, OH 43210, USA

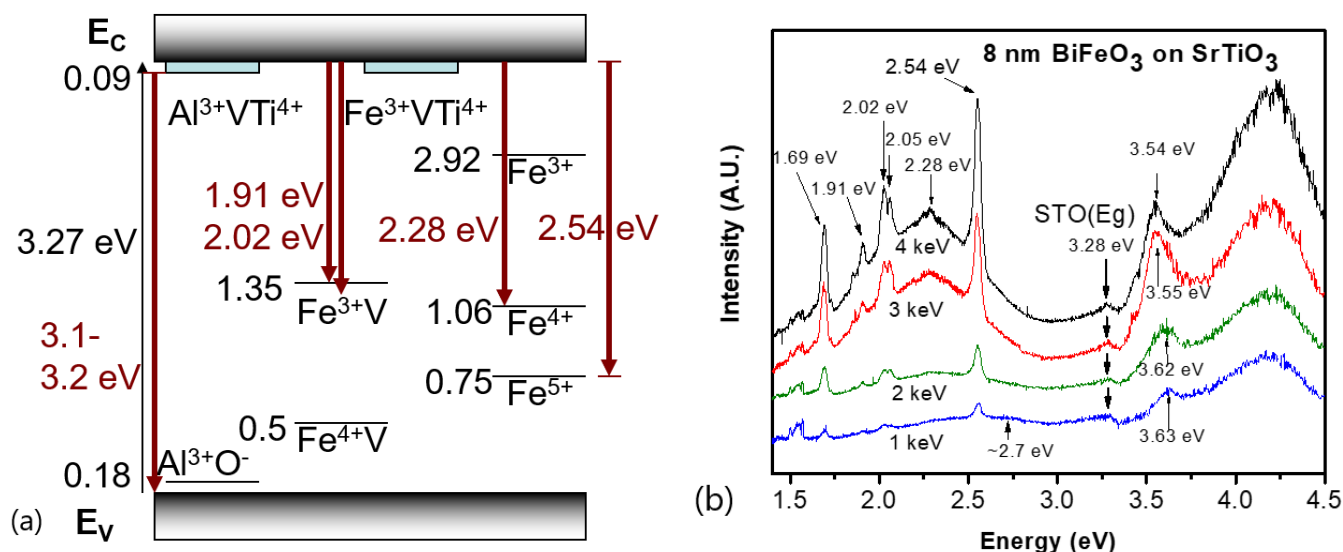


Fig. S1. (a) Optical transition energies for Fe and Al impurities in SrTiO<sub>3</sub> from the conduction band to Fe-related defect levels at energies indicated above the valence band. After Morin and Oliver.<sup>1</sup> (b) DRCL spectra for BiFeO<sub>3</sub> on SrTiO<sub>3</sub> showing sharp emission peaks 1.91, 2.02, 2.28, and 2.54 eV corresponding to Fe impurity transitions illustrated in (a).

Figure S1 illustrates the correspondence between energy levels of Fe-related defects in the SrTiO<sub>3</sub> band gap and DRCL peaks observed in bulk SrTiO<sub>3</sub>. Figure S1(a) shows energy levels relative to the valence band  $E_V$  that are derived from data in the literature, specifically measurements of thermally stimulated current, electrical conductivity, and thermoelectric effect.<sup>1</sup> Figure S1(b) shows depth-resolved cathodoluminescence (DRCL) spectra for an 8 nm thick deposited BiFeO<sub>3</sub> film on commercial SrTiO<sub>3</sub>. With increasing incident electron beam voltage  $E_B$ , a set of relatively sharp peak features emerges below 3 eV that correspond to excitation of the SrTiO<sub>3</sub> substrate.

Features at 1.91, 2.02, 2.05, 2.28, and 2.54 eV that correspond to transitions to states below the conduction band  $E_C$  match closely with the published energy level positions above  $E_V$ . The narrow linewidths of these cathodoluminescence features contrasts with the broader linewidth BiFeO<sub>3</sub> and SrTiO<sub>3</sub> band gap emissions shown at 2.7 eV and higher photon energies. The pronounced intensities of these features are also in contrast to the broader features and energies corresponding to the intrinsic SrTiO<sub>3</sub> defects reported in this study. Their high intensities in DRCL spectra may be the result of the overlayer growth of (001) BiFeO<sub>3</sub>, which involved deposition of Fe on clean SrTiO<sub>3</sub> by ultrahigh vacuum sputtering.<sup>2</sup> Their energies differ significantly from those of the intrinsic defects as does their appearance in multiple charge states.

---

<sup>1</sup> F.J. Morin and J.R. Oliver, Phys. Rev. **B8**, 5847 (1973).

<sup>2</sup> A.J. Hauser, J. Zhang, L. Mier, R.A. Ricciardo, P.M. Woodward, T.L. Gustafson, L.J. Brillson, and F.Y. Yang, Appl. Phys. Lett **92**, 222901 (2008).